Vessel recovery using ultrasound localisation microscopy: An in silico comparative study between minimum variance and delay-and-sum beamformers

Vasiliki Voulgaridou, Barbara Nicolas, Steven Mcdougall, Lachlan Arthur, Georgios Papageorgiou, Mairead Butler, Evangelos Kanoulas, Konstantinos Diamantis, Weiping Lu, Vassilis Sboros

Ultrasonics 145 (2025) 107451

Contents lists available at ScienceDirect

Ultrasonics

journal homepage: www.elsevier.com/locate/ultras

Vessel recovery using ultrasound localisation microscopy: An *in silico* comparative study between minimum variance and delay-and-sum beamformers

Vasiliki Voulgaridou [a], Barbara Nicolas [b], Steven McDougall [c], Lachlan Arthur [d], Georgios Papageorgiou [d], Mairead Butler [d], Evangelos Kanoulas [e], Konstantinos Diamantis [f], Weiping Lu [d], Vassilis Sboros [d,*]

[a] Translational Healthcare Technologies Team, Centre for Inflammation Research, Queen's Medical Research Institute University of Edinburgh, United Kingdom
[b] Univ Lyon, INSA-Lyon, Université Claude Bernard Lyon 1, UJM-Saint Etienne, CNRS, Inserm, CREATIS UMR 5220, U1206, F-69621 Lyon, France
[c] Institute of GeoEnergy Engineering Heriot Watt University Edinburgh, United Kingdom
[d] School of Engineering and Physical Sciences Heriot Watt University, Edinburgh, United Kingdom
[e] Janssen Pharmaceuticals R & D, High Wycombe, United Kingdom
[f] Institute for Digital Communications University of Edinburgh, Edinburgh, United Kingdom

ARTICLE INFO

Keywords:
Ultrasound beamforming
Microbubble-tracking
Ultrasound contrast imaging
Super-resolution ultrasound
Ultrasound localisation microscopy
Minimum variance

ABSTRACT

The use of particle localisation and tracking algorithms on Contrast Enhanced Ultrasound (CEUS) or other ultrasound mode image data containing sparse microbubble (MB) populations, can produce super-resolved vascularization maps. Typically such data stem from conventional delay and sum (DAS) beamforming that is used widely in ultrasound imaging modes. Recently, adaptive beamforming has shown significant improvement in spatial resolution, but its value to super-resolution image analysis approaches is not fully understood. The *in silico* study here evaluates the performance of combining minimum variance beamformers (MV BF), established to provide improved lateral resolution, compared to DAS BFs with single particle detection. The isolated effect of a range of simplified image-affecting factors such as flow profile, pulse length, noise, vessel separations and data availability is considered. The study aims to assess the vessel recovery performance using the different beamformers and investigate the link with MB detection and localisation. The MV BF was shown to provide improved microvessel position accuracy compared to conventional DAS BFs. In particular, vessel separations between 0.3–4 λ provided superior localisation uncertainty with the MV. In addition, for a separation of 0.36λ, vessel recovery was achieved with both methods but the use of MV eliminated artifacts that appear as additional vessels. These results were found to be linked to improved MB detection and localisation for the MV BF, which is proposed as suitable for testing in Ultrasound Localisation Microscopy (ULM) imaging using patient data.

1. Introduction

A key focus of medical imaging research, including ultrasound imaging, is to improve resolution in order to provide more detailed images, that are a 'closer look' into the pathophysiology of diseases and thus benefit clinical diagnosis. There is a series of non-communicable diseases (NCD) – including cardiovascular disease, diabetes, cancer and neurodegenerative conditions such as Alzheimer's and Parkinson's – that have been shown to incur changes in the microcirculation [1–3]. It is hypothesized that the understanding and treatment of these illnesses would benefit from a diagnostic tool capable of directly mapping the microcirculation which is direct pathophysiological information. The advent of super-resolution ultrasound imaging (SRUI) shows, unlike all other medical imaging, significant potential in directly mapping the dynamics of microvascular networks, thus promising a prompt and more detailed histology-like diagnostic imaging solution. While a significant amount of work concentrates on image analysis, there is less research on signal processing. Fundamental array processing work [4–11] has focused on adaptive beamforming (BF) and established its potential for improving image quality and spatial resolution [6–11]. More recently, a

* Corresponding author.
E-mail address: V.Sboros@hw.ac.uk (V. Sboros).

https://doi.org/10.1016/j.ultras.2024.107451
Received 26 June 2023; Received in revised form 26 August 2024; Accepted 29 August 2024
Available online 30 August 2024

number of studies investigated adaptive beamforming aiming to address their computational complexity [12–14], improve robustness [15,16], and image quality [17–24] in the context of structural imaging. However, there is little work in coupling such methods with super-resolution image analysis [25–27].

SRUI vascular maps are generated by means of detection, localization and often tracking of intravenously injected ultrasound contrast microbubbles, that remain in the vascular space, and are typically detected utilizing contrast enhanced ultrasound imaging (CEUS) imaging modes. Such modes deploy pulse modulation such as pulse inversion [28,29] and/or amplitude modulation [30], in combination with the conventional DAS BF [31,32]. It has been known for some time that the scattering from ultrasound microbubble contrast agents using CEUS modes can be detected individually [33]. However, to our knowledge, the implications of using a BF that has the potential to improve spatial resolution and is known to resolve more particles in the ultrasound image, such as the minimum variance (MV) or other adaptive BF, are not understood in terms of benefit to the mapping of vessels particularly over the DAS established BF. Yan et. al [27] are closest in showing an association between super-resolution image quality improvement and the performance of an adaptive BF, with a demonstration of fewer spurious microbubble detections, increase in true detections and clearer vessel profiles compared to the DAS. However, despite the improved resolution of adaptive BFs compared to the DAS, there is little improvement in the resolution of the final SRUI map that is attributable to the adaptive BFs, and the origin of erroneous echoes is difficult to explain in the absence of ground truth. Similar *in vitro* results are demonstrated by Tasbaz and Asl [25] where the BFs provide very similar localization uncertainty, and no quantifiable resolution improvement in the SRUI maps. It is important to note that, similar to the DAS, the MV BFs are also diffraction limited, and it has been shown that the theoretical limit for resolving two scatterers is around λ [34].

These two publications show that the association of SRUI imaging quality and adaptive BF performance is complex, multi-factorial and poorly understood. Indeed, it has been shown that an adaptive BF, namely the MV BF, can provide a 24-fold smaller Full Width at Half Maximum (FWHM) (0.08λ) for a single scatterer compared to the DAS [34,35]. However, the advantage of applying the MV BF or any other adaptive BF is not clearly evidenced in the literature in super-resolution maps. First, in the context of ULM, it has not been demonstrated that the localization uncertainty is superior for the MV or any adaptive BF compared to DAS. The work by Tasbaz and Asl [25] shows that all beamformers provide similar ULM localization uncertainty. It is established that localization uncertainty is dependent on microbubble signal-to-noise ratio and less so on resolution [36,37], which suggests that a smaller PSF does not guarantee better localization, and may explain the above performance similarity between different beamformers. Second, in theory when two scatterers are close to each other they cannot be super-resolved, as it has been shown that the separation of two scatterers is challenging below one λ for the MV and 2λ for the DAS [34,35]. This is attributed to PSF 'growth' in the vicinity of another depending on their distance, effectively depending on the degree of side lobe interaction. Phantom work has confirmed that the experimental minimum distance detected between two scatterers using the MV was 1.21λ [34]. This means that adaptive BFs are not yet capable of resolving two adjacent particles beyond the diffraction limit (i.e. at distances closer than λ/2), also confirmed by Zhang et al [24]. Third, MB vicinity has been shown to distort/tilt PSF shape [34], which may significantly compromise localization precision. In addition, it is established that the imaging is performed in the near-field of the ultrasound array which results in variable PSF. Variations in tissue speed of sound and attenuation, their interaction with transmission and receive setting and limitations of display processing (i.e. averaging, interpolation etc) generally lead to alterations of PSF shape. The experimental results have shown that the MV have slightly bent PSF (Fig.10 of [34]), that may result in localisations outside the PSF area, a significant systematic error specific to the MV BF. Fourth, the MV image resolution deteriorates as the number of scatterers increases. As mentioned above experimental phantom work has shown no resolution advantage of the MV in imaging continuous structures [22] and best performs with a few isolated scatterers [35]. Indeed, a number of studies show a large MV performance variability [34,35,38–41], mainly attributed to its dependence on the receive data amount, as it is established that the MV performance is data dependent, and in the context of imaging real structures it has not demonstrated a significant resolution advantage over other BFs. In other words, the smaller PSF of isolated particles provided by a number of adaptive beamformers has not been shown to lead to a resolution advantage for super-resolution imaging. Further, the practical aspect of mapping super-resolved microvascular networks involves a trade between microbubble concentration and data acquisition time [42–44], that directly impacts on patient examination time and motion compensation requirements, as large concentrations may reduce acquisition time but may also lead to deterioration of the performance of the beamformers and subsequent localization precision.

The current study assesses the impact of combining adaptive beamforming and ULM on blood flow scenarios where factors other than resolution may affect the image quality. Specifically, it is important to understand whether the smaller PSF of the MV BF compared to the DAS leads to improved capacity to resolve vessels. Here, the focus is on a simplified *in silico* flow phantom consisting of two adjacent parallel vessels and with image settings aiming to help understand the origin of the possible benefits of adaptive beamforming on vessel reconstruction and resolution. Parameters such as the distance between the two vessels, the pulse length, which impacts axial resolution, noise and the number of particles are investigated. The microbubble concentration used allows sparse and isolated microbubbles, but is relatively high in order to reduce acquisition time, and thus providing more realistic imaging conditions that would likely generate challenges in microbubble detection and localization. In order to address this BFs that are well reported and established were utilized, including the state-of-the-art DAS and the well documented MV BF. The aim is to disentangle the factors that contribute to better ULM maps and determine whether adaptive beamforming is theoretically justified for development in the context of super-resolution imaging.

2. Methods

2.1. Beamforming

The experimental design utilizes an *in silico* evaluation of two different beamformer families, the state of the art delay and sum (DAS) and the minimum variance (MV) adaptive one. Each has two versions, namely, the DAS with uniform spatial apodization (DAS boxcar) and DAS with a Hamming spatial apodization (DAS Hamming), the MV BF in the temporal domain (MV Temporal) and the MV BF in the frequency domain (MV Subband) all of which are well documented [34,35]. These will be investigated in terms of ULM imaging output performance for vessel recovery.

Minimum Variance

The MV beamformer has been previously optimized for imaging point scatterers [35,38] with additional studies assessing the impact of MV parameters for point scatterers [7,40,45]. This information was used to maximise the MV performance in the ultrasound simulations. The techniques applied on the data presented here were a diagonal loading [7] and a forward–backward averaging [45] which allows the inversion of the sample covariance matrix for a larger transducer sub-array length value, thus increasing the maximum achievable resolution.

2.2. Phantom design

The phantom designed for this experiment using *numPTI* software [46] comprised a system of two 50 μm diameter parallel vessels placed

at different lateral separations. Complexity in the vessel shape and arrangement was avoided as this arrangement ensured a characterization of all the parameters involved. The MBs were flowing in opposite directions at a constant flow rate of $5x10^{-10}$ m^3/s and were injected randomly into one of the two vessels at a rate of 10 particles per second for the vessel system. The randomness ensured variability in MB relative position. Fig. 1 shows that this design provides (i) single MBs in relative isolation from other MBs, (ii) lateral-pairs of MBs at various separations, (iii) clusters of MBs in one of the two vessels with a single MB in the other vessel at the same depth, and (iv) clusters of MBs in one vessel at a similar height to clusters of MBs in the other vessel. The two vessels were placed at lateral separations, ranging from 70 μm to 1500 μm (0.36–7.8λ) covering distances from below the diffraction limit to adequate for standard resolution to enable vessels discrimination. In addition, the larger distances between vessels ensure that the scatter from MBs flowing in the different vessels will not interact and thus their signal will be similar to that of single scatterers, thus enabling ideal conditions for vessel identification.

In the MB flow simulations, the MBs are represented by dimensionless 'particles' injected in the center of the vessels and flowing at a set flow rate. The resolution and vessel recovery performance assessment is linked to MB localization and vessel separation and does not depend on vessel width. The particles only flow along the central streamline of the vessel. The radius of the vessel is used for the calculation of the flow rate, i.e., determines how quickly the particles will traverse the vessel. The MB positions are used as Ground Truth (GT) information against which the performance of the detection algorithm could be evaluated by means of ULM. A preliminary test on a single vessel was performed to confirm BF performance for the *in silico* vessel design and, thus, help assess the effect of the additional vessel.

Fig. 1. Phantom of two linear vessels (red) for four different lateral separations: 100 μm, 200 μm, 400 μm, and 1000 μm. The white dots are simulated MBs flowing through the vessels. The snapshot shows typical MB grouping behavior for the chosen flow parameters.

2.3. US image generation

The MB flow simulation generated a dataset of 300 consecutive 2D images/time-frames. One hundred consecutive time frames were chosen representing steady MB flow of a typical ULM acquisition protocol, i.e. the wash-in and wash-out phases of the injection were excluded. The simulated US data were generated using Field II [47,48]. It is recognized that microbubble scatter is nonlinear and is challenging for detection and localization algorithms, but here it is the comparison of a number of parameter ranges that are tested and Field II is an established simulator that ensures an even and fair comparison platform. Every MB was assigned an amplitude value from a range of values consistent with the particle in the frame sequence. This was to introduce a challenge for the detection and localization algorithms. The Field II synthetic aperture (SA) [49] transmission protocol was used with central frequency of 8 MHz ($\lambda = 192.5$ μm) however, only the central element, i.e. element 64, was used for the transmission and all the elements were used for the receive. Thus, the emitted spherical wave sufficiently covered the vessel phantom area for a depth ranging between 52–80 mm. The detailed imaging parameters can be found in Table 1. The received data were processed with the four BF methods: DAS boxcar, DAS Hamming, MV Temporal and MV Subband developed by Diamantis et al. [34]. In an initial experiment, the images were generated without noise for each vessel separations and for three different transmission pulse lengths that were uniformly weighted: 2 cycles, 8 cycles, and 16 cycles. While the MV BF improves lateral resolution, the reduction of pulse length improves axial resolution. Thus, changing the pulse length will help elucidate the impact of axial resolution variation on super-resolution maps. In addition, this experiment will help understand the impact of the MV BF on super-resolution maps, which typically improves lateral resolution. Once the optimal transmission pulse length was determined, the experiment was performed introducing white noise on the echo data resulting in SNR ranging from 0 – 25 dB.

2.4. Image analysis

The MB detection, segmentation and localization was performed using the ULM methodology in [50]. Briefly, for the detection the MBs were distinguished from the background using marker-controlled watershed segmentation [51] and the segments of MBs were selected using a series of criteria such as the peak intensity, the minimum/maximum size of the segments. After the identification of a region as a MB, the localization process estimates its position using the intensity weighted centre of mass method. The algorithm's input parameters, i.e., minimum/maximum particle size and intensity of each region, were tuned in each dataset to optimize the detection.

2.5. Evaluation using the ULM data output

The GT location of each MB, in each frame, was used for the performance evaluation of the MB detection and localization process via the

Table 1
Field II imaging parameters.

Transducer Type	Linear Array
Transducer Element Pitch	110 μm
Transducer Kerf	35 μm
Transducer Element Height	6 mm
Centre Frequency f_0	8 MHz
Sampling frequency, f_s	100 MHz
Bandwidth	60 % fractional
Speed of sound	1540 m/s
Wavelength, $\lambda = c/f_0$	192.5 μm
Excitation Pulse	2-cycle, 2c/8c/16c sinusoid at f_0
Number of elements per emission	1
Number of receiving elements	128

following metrics: a. True detection (TD) rate (percentage of correct detections to all GT MBs), b. Spurious events rate (percentage of detections to all GT MBs, that do not correspond to GT MBs), c. Missed events rate (percentage of MBs that were not detected) and d. Localization Uncertainty (LU) which is calculated as the root mean squared error of the distance of each localization from the GT, which applies only to TDs. The number of detections was used to construct parametric maps of the MB number, where each pixel value is the count of all detections throughout the frame sequence. As the vessels are straight, the MB localizations in each vessel were used to generate the vessel profile histogram. Note, that the ground truth vessel has negligible diameter and thus, the vessel width is generated by the localization error, which is also partly the case for *in vivo* results. In addition, the localization error may be both random, due to noise, and systematic due to adjacent MB interaction. It was found that the Gaussian was a reasonable fit to the vessel profile histogram and that the mean value of the fitted Gaussian μ_i provided an excellent estimate of the vessel position p_i:

$$p_i = \mu_i \tag{1}$$

This enabled the estimation of the vessel separation which was compared with the actual separation defined by the phantom design. In addition, the FWHM of each vessel was estimated as the apparent vessel width. As the distributions of the vessel profiles are considered normal the standard deviation of their location is given by:

$$\sigma_i = FWHM/\sqrt{(2\ln(2))} \tag{2}$$

The particles are only flowing along a central streamline in the GT flow simulation therefore σ_i is the error of the estimated vessel position p_i. For two neighboring vessels of positions $p_1 \pm \sigma_1$ and $p_2 \pm \sigma_2$ their distance d_{12} is:

$$d_{12} = |\mu_1 - \mu_2| \pm \sqrt{\sigma_1^2 + \sigma_2^2} \tag{3}$$

3. Results

3.1. Single vessel

This initial test was conducted on a single vessel phantom. Small variations in concentration and amplitude value are generally the most significant cause for variability in the localization uncertainty. Fig. 2 shows the vessel profiles of the four BFs: DAS boxcar, DAS Hamming, MV Temporal, MV Subband along with the vessel $p_i \pm \sigma_i$ of the histograms.

Table 2 shows the results for all the BFs for the single vessel phantom and the FWHM for a single PSF at depth of 63.6 mm. All the detections are classified as TD and there are no spurious detections or missed events. The single PSF FWHM measurements confirm previous results [34] where the MV BF shows an advantage in reducing the size of a

Table 2
ULM Evaluation metrics for single vessel phantom using the four BFs.

	DAS Boxcar	DAS Hamming	MV Subband	MV Temporal
FWHM@ z = 63.6 mm	450 μm (2.33λ)	710 μm (3.69λ)	80 μm (0.41λ)	84 μm (0.44λ)
TD (%)	100	100	100	100
SPR (%)	0	0	0	0
Missed (%)	0	0	0	0
LU (μm)	17.9 (0.09λ)	15.6 (0.08λ)	15.6 (0.08λ)	22.9 (0.12λ)
σ_i (μm)	2.5	2.0	1.8	2.0

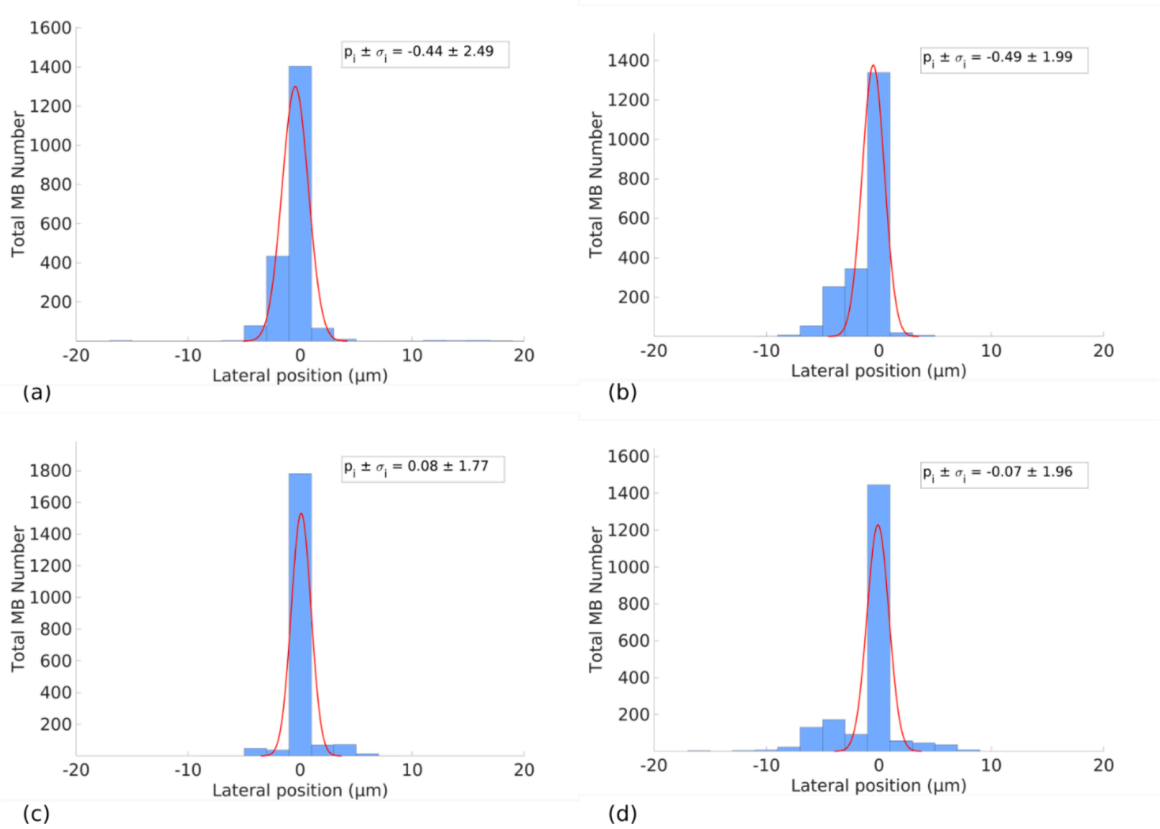

Fig. 2. Profile of single vessels as determined by MB localizations for the four different BFs, (noiseless data sets): a) DAS boxcar, b) DAS Hamming, c) MVS, d) MVT.

single PSF more than 5-fold compared to DAS BFs. However, all the BFs provide similar localisation uncertainty ranging between 0.08–0.12λ and similar vessel width (σ_i) between 1.8–2.5 μm. This shows that there is no advantage in using the MV over the DAS BF for the localization of a single vessel and when MBs are well separated. This demonstrates that the PSF size alone (i.e. FWHM) does not determine localization performance, and confirms that other factors such as SNR and goodness of fit to localization model are key to localization uncertainty [52]. It is important to note that vessel location p_i seemed slightly superior for MV beamformers (0.07–0.08 μm) compared to the DAS (0.44–0.49 μm). This is associated to the lack of symmetry of the higher uncertainty localisations, shown in the histograms, for the DAS beamformers, likely attributed to different positioning of the PSF in the simulator (i.e. not every single PSF of each beamformer is centered at the same position).

3.2. *Effect of transmission pulse length in two vessels*

Images obtained by the four BF methods are shown in Fig. 3a, b for a transmission pulse length of 2 and 16 cycles respectively. The vessel separation is 1000 μm (5.2λ) as it provides minimal interaction between the MB echoes, between the two vessels, for all the BFs and therefore enables the isolation of the assessment of the transmission pulse length effect (i.e. axial interaction). The example frame of Fig. 3 shows both single isolated MB echoes, e.g. z = 73 mm (red arrow), overlapping echoes laterally, e.g. z = 58.5 mm (green arrow), as well as clusters of overlapping echoes both laterally and axially, e.g. z = 70.5–71.5 mm. Fig. 3c,d show the respective GT positions (blue dots) of the MBs along with the localisations using the different BFs (red crosses).

Generally, the use of longer cycles elongates the PSF. This is evident in the three examples mentioned before: the isolated event marked by a red arrow at 73 mm, the MB pair marked by a green arrow at z = 58.5 mm, and the cluster of events at depth of 70.5–71.5 mm. Increasing the pulse length increases the axial interactions of neighboring MBs leading to a compromised MB detection and localization processes. This is evident through a comparison of Fig. 3c and Fig. 3d where an increase in spurious events is noted. Further, each BF produces a different lateral pattern which has an effect on the detection and localization performance. The elongated PSFs increased the probability of lateral interaction: the increased PSF area can skew the detections of MBs which are in the second vessel but not at the same depth. A pulse length that doesn't generate this elongation effect decreases the probability of skewed particle appearance which consequently decreases the localization uncertainty.

The overall performance of the three pulse lengths that were studied in combination with each of the four BFs is captured in Fig. 4 where the percentage of TD as a function of the percentage of spurious events is plotted. All BFs are contained within each pulse length grouping resulting in 16 data-points per pulse length. There is a correlation between TD and spurious events, which is more pronounced for pulse lengths of 8 and 16 cycles (black and blue markers). This trend is not

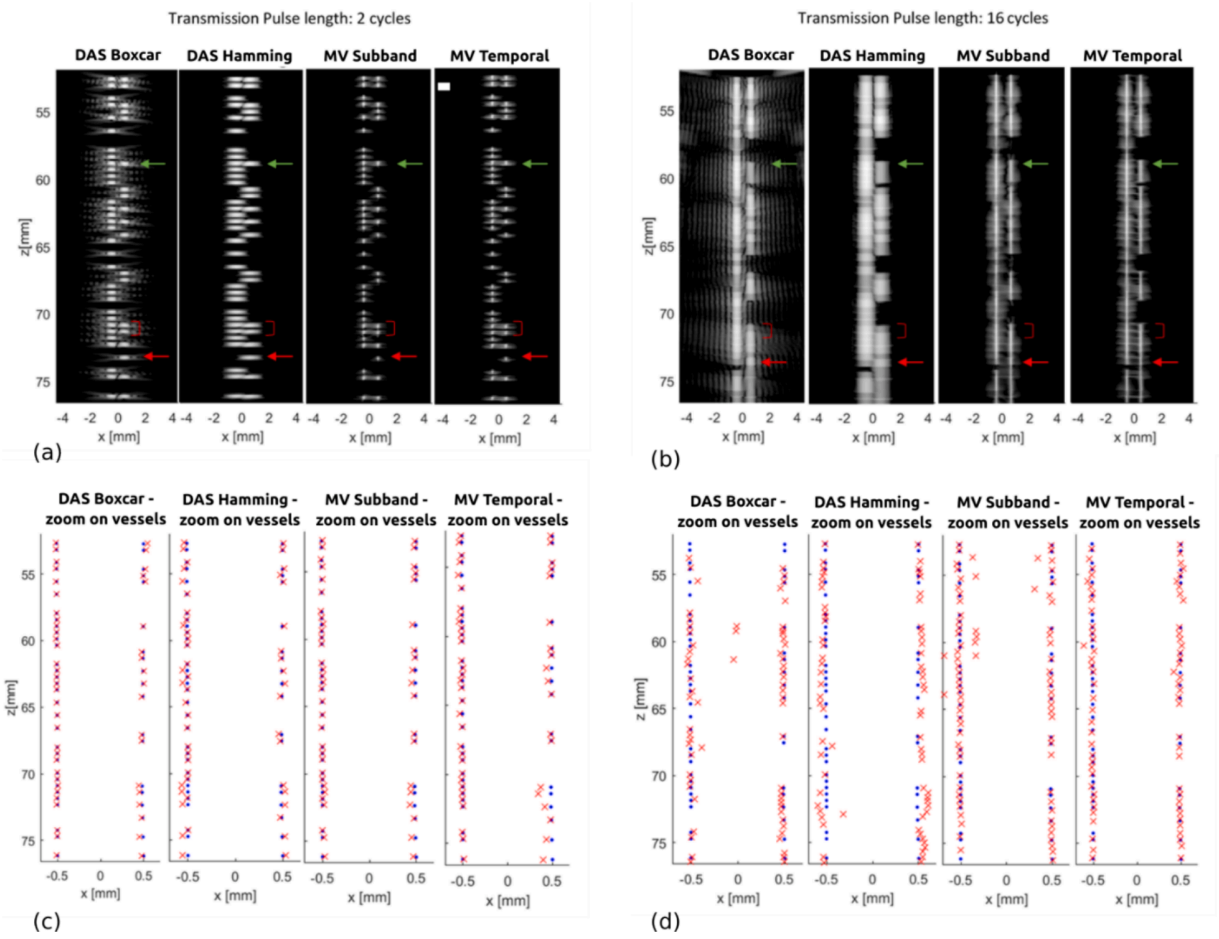

Fig. 3. Selected *in silico* CEUS time frame of the same GT positions for a vessel separation of 1000 μm (5.2λ) (a) BF images for transmission pulse length of 2 cycles. The green arrow shows a pair of MBs at the same depth, the red arrow shows an isolated MB, and the red bracket shows a cluster of MBs. (b) same time frame BF for pulse length 16 cycles (c)The GT positions of the MBs (blue dots) corresponding to the time frame (a). The red crosses are the ULM detections, (d) GT positions and detections of time frame (b).

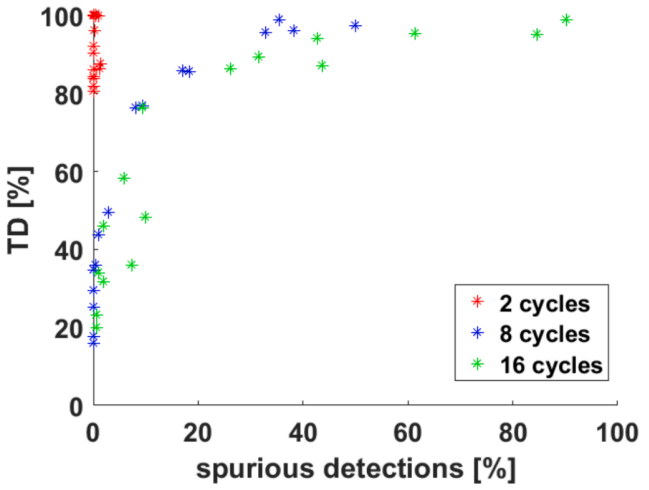

Fig. 4. Percentage of correctly detected MBs versus percent spurious detections for the three transmission pulse lengths. For a length of 2 cycles the ratio of correct detections versus spurious is optimal whereas for longer transmission pulse lengths there is an increasing trend. Every cycle-length parametric curve consists of 16 data points from 4 different vessel separations beamformed by the 4 different BFs.

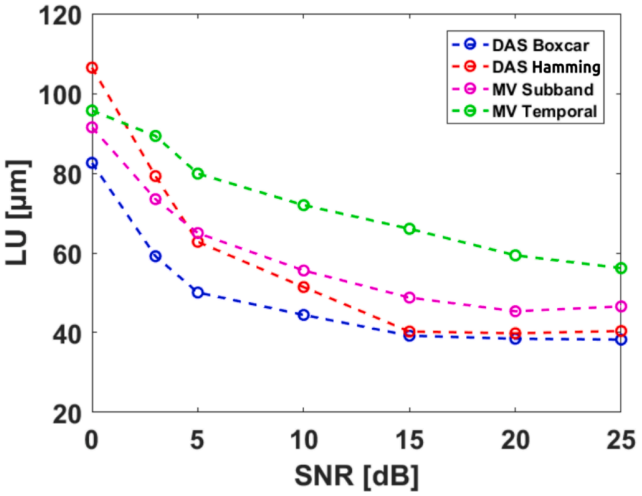

Fig. 5. LU versus SNR at 1000 μm vessel.

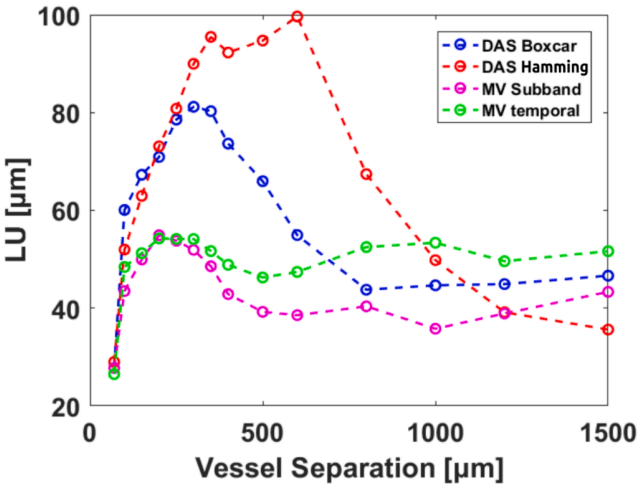

Fig. 6. LU versus vessel separation for the different BFs in the absence of noise. Vessel separation ranges between 70 μm −1500 μm.

apparent for the 2 cycle pulse (red markers) since the spurious events are significantly lower (less than 1.5 %). Furthermore, the TD rate is higher than 80 % for all the BF cases where 2 cycle pulses were used.

These results show that, given a realistic MB concentration, the use of longer transmission pulses is likely to generate a significant increase in spurious events and lower numbers of TDs. Thus, longer pulses are not suitable for ULM processing as they may increase noise, distort vessels and introduce artefacts. To alleviate this problem a significant reduction of the MB concentration may be required, which, in a clinical setting, results in an increase in acquisition time. This may not fully resolve the problem as, in reality, vessels are mostly not parallel, and their arrangement may generate PSF interactions for the longer pulse durations. For these reasons the lowest duration of 2 cycles was chosen for the rest of the work in this study as it presents the optimal choice for further investigation.

3.3. Effect of noise on LU

The effect of noise was studied for the 1000 μm vessel separation dataset for a SNR range between 0 dB, where the MBs are hardly discernible from the background, and 25 dB where MBs are clearly displayed[53]. The results are shown in Fig. 5. The introduction of noise increased the number of spurious events and most importantly it had an effect on LU. At an SNR level of 25 dB, the LU takes the lowest values ranging from 42 to 60 μm for all BF methods, which converge to the LU values of the noise-free experiment.

This result shows that the LU and LU deterioration are fairly similar amongst the four BFs at different noise levels, corroborating to the fact that SNR is a key determinant of localization precision. The exception is the LU deterioration is greater on the images generated by the MV Temporal due the smaller PSFs, that may result in a reduced SNR or worse fit to the localization model. The other three BFs were very similarly affected by noise. The larger PSFs of DAS Boxcar, that also presents the most consistent shape, provide the best LU values in the lowest SNR (0–10 dB).

3.4. Effect of BF method for different vessel separations

The localization performance for the four BF methods is evaluated in Fig. 6 which shows the LU of the BFs for vessel separations ranging from 70 μm to 1500 μm. The MV BFs provide LU around an average, which lies at 45 μm for the MV Subband and 50 μm for the MV Temporal. The DAS BFs demonstrate localization performance comparable to the MV for vessel separations above 1000 μm, which can be considered as the lateral distance that provides well separated MBs for all BFs. Note, that, compared to Fig. 5, the MV subband at this vessel distance in Fig. 6 appears to have slightly lower LU while both DAS have slightly higher, while the MV temporal consistently has the highest LU. This is because the results in Fig. 6 stem from a noiseless experiment, which favours both MV BFs in terms of PSF appearance, that provide an improved fit to the localization model. The small compromise of the DAS derived LU is due to their large PSF, which, in the existence of random noise, slightly reduces the significance of PSF interaction between MBs and results in a slightly improved fit to the localization model (even at 25 dB SNR in Fig. 5).

The BFs' performance also appears to converge for the smallest vessel separations below 100 μm: at these lateral separations there is almost complete overlap between the MB echoes and the resulting LU is close to that of a single MB. This occurs because the PSF overlap leads to the detection of two closely positioned particles as a single event. In such ULM validation the detection would typically be compared to one of the two GT positions of the pair, while the other GT position would be

recorded as a missed event. As a result, the localization of the detected event may lie between the two vessels, hence the LU is smaller than the 100 μm separation. A consequence of this effect is that one of the two vessel positions is recorded with high accuracy each time and the accumulation of such events can lead to correct vessel localizations even though a single pair of particles is not typically resolved by ULM. This happens at the expense of missed events which explains the similar LU performance for the smallest and the largest vessel separations. Specifically, the average percentage of missed events for a separation of 70 μm is 31.9 % while for a separation of 1500 μm it is 1.7 %.

The lateral vessel separations for which the use of MV methods provides a clear benefit in LU performance over the DAS are between 200 μm and 800 μm. These are the critical separations for which the DAS PSFs overlap laterally for paired events but the MV PSFs show a smaller degree of overlap. Such merged MBs as well as others that interact, which may be at slightly different axial positions over these vessel distances, create increased uncertainties in LU for the DAS BFs compared to the MV BFs. For this range of separation the level of overlap is inversely proportional to the separation reaching an almost complete overlap for GT separation below 100 μm for both DAS and MV. This result is a consequence of our previous finding that at this distance range two MBs appear merged and cannot be separated [34]. Above the nominal vessel distance of 800 μm there is no longer overlap, the PSFs are easily distinguished in the segmentation processes.

For a vessel pair at a distance of 70 μm (0.36λ), the different BFs were evaluated using the MB number maps and vessel profile histograms (Fig. 7). Fig. 7 shows that for this separation, which is below the λ/2 mark for super resolution [36], the vessels are identified as separate structures i.e. super resolution is achieved.

In both DAS vessel profiles the two peaks correspond reasonably well to the position of the original vessels. The difference in the height of the peaks is due to the different number of localisations. However, there is a significant number of spurious detections that produce an artefact, erroneously identified as a vessel. For DAS Boxcar the additional peak is found at $p_i = 1.2 \pm 15.79$ μm and for DAS Hamming it is found at $p_i = -1.2 \pm 11.21$ μm. In the profiles of MV Temporal (MVT) and MV Subband (MVS) the vessels are easily discernible, while their distance is better than the one of DAS Hamming. In summary, all BFs identify the existing vessels with artefacts mostly present in DAS, related to the interference between closely spaced MBs. The same effect of an additional vessel is also observed for a vessel separation of 100 μm. Larger separations did not produce this vessel artefact for any of the BFs.

Table 3 shows a summary of the estimated values of vessel separations for all BF methods. The estimated separation is in good agreement with the actual value for all BF methods. The MV subband appears to perform well for 200 and 400 μm vessel separations although this is not statistically significant.

3.5. Noise and vessel profiling

The performance of the BFs in defining and resolving vessels was tested for images with different noise levels for a nominal vessel separation of 1000 μm. Fig. 8 shows that while the vessel separation fluctuates around the nominal value for all BFs, the separation uncertainty is clearly correlated to the SNR level. Above 15 dB SNR the separation estimation converges to an accuracy below 40 μm for all BFs, other than the MV Temporal. This behavior is consistent with the LU performance and is attributed to the specific MV Temporal PSF characteristics raised

Table 3
Estimated vessel separation (μm), (noiseless data set).

	DAS Bx	DAS Hn	MVS	MVT
GT_{70}	69 ± 24	64 ± 40	67 ± 39	71 ± 35
GT_{100}	101 ± 29	101 ± 13	97 ± 23	103 ± 24
GT_{200}	206 ± 19	208 ± 21	202 ± 19	205 ± 20
GT_{400}	425 ± 47	407 ± 26	400 ± 24	410 ± 23
GT_{1000}	993 ± 27	1014 ± 30	980 ± 17	1005 ± 23

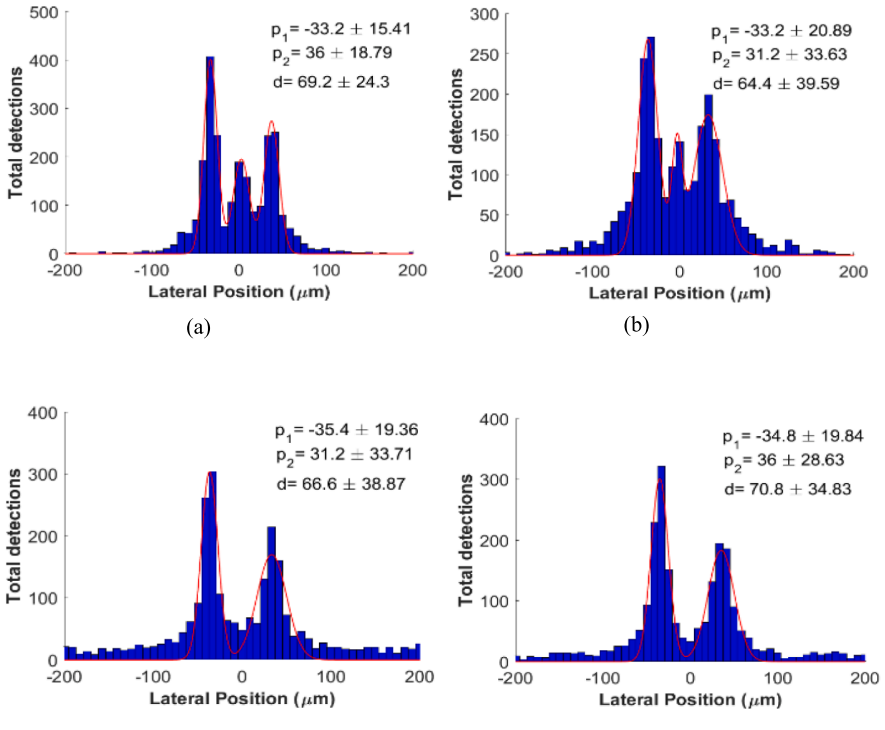

Fig. 7. Resolution of vessel-pair at a separation of 70 μm(0.36λ) (noiseless): a) DAS Boxcar, b) DAS Hamming, (c) MVS, (d) MVT.

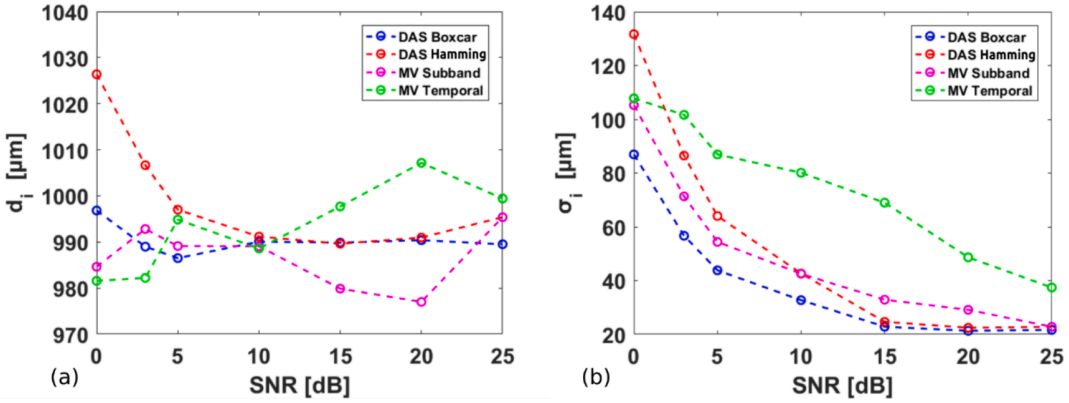

Fig. 8. The effect of noise on vessel profiling. The profiling process was applied on a nominal vessel separation of 1000 μm and the graphs show (a) the estimated separation, (b) the error of the estimated separation.

above. In the light of this Fig. 8a provides reasonable fluctuations within the error displayed in Fig. 8b.

3.6. Data amount

The difference in vessel location p_i performance and uncertainty σ_i between the left vessel and right vessel in Fig. 8 is also attributed to the different number of MBs recorded in each vessel, which suggests that the number of MBs impacts on vessel localization and separation estimation uncertainty. Fig. 9 shows the estimated vessel separation d_i and its uncertainty versus different sizes of detection datasets. Note that the concentration of MBs was kept the same to isolate the effect of data availability for the same MB flow conditions. The data of Fig. 9 are for a nominal vessel separation of 1000 μm that typically provides minimal interference between MBs. As expected the separation estimation is erroneous and the separation uncertainty is suboptimal for MB numbers lower than 20 for all BFs. For the DAS Boxcar more than 400 MBs are required to converge the separation estimation to the GT values, it is likely to be the only beamformer that provides some PSF interaction at this vessel separation due to the higher amplitude sidelobes compared to all the others[54]. On the other hand both MV BFs show that even 20 MBs are adequate to provide convergence to correct separation estimation.

4. Discussion

In order to define and super-resolve a microvessel in the vicinity of others using ULM, an adequate amount of good quality MB echoes are required. Accurate information on the vessel width, the flow pattern within it (e.g. laminar or not) and its dynamic information (e.g. blood speed) can be obtained. In this paper we investigated the effects of detection and localisation accuracies of images generated by the MV and DAS BFs in an effort to understand their impact on defining and resolving vessels in proximity. To our knowledge it was shown for the first time that an adaptive BF, such as the MV, has an advantage for improved vessel definition and vessel resolution compared to a DAS BF specifically in the approximate distance range between 0.3 and 4λ. These results are complemented with good accuracy in vessel location, and achieved with only a small number of MBs, which implies shorter video loops and acquisition time. These advantages of the MV BF may be crucial for a consistently optimal performance of ULM across the image that is not data dependant. This is relevant to the early detection of solid tumours that often differ from normal tissue due to the onset of angiogenesis at this specific spatial scale [55]. These neo-vessels range between a few tens to a few hundreds of micrometers in diameter [50]. Further, compared to normal tissue the tumour neovasculature is often very closely spaced. The results here show that it is in these areas that the DAS BFs are likely to underperform, in radiological applications (i.e. with similar λ) thus misrepresenting the microvascular density and flow, while the MV BF may help differentiate these microvessels thus improving microvascular mapping at a scale relevant to tumour diagnosis.

The simulations undertaken here explain the reduction of artefacts or erroneous image features of the MV BF compared to DAS that is shown in experimental studies. It is recognised that the principle of SRUI processing requires adequate microbubble sparsity in order to localise them beyond the diffraction limit and thus provide vessel maps of analogous image quality. The increase of concentration increases the likelihood of

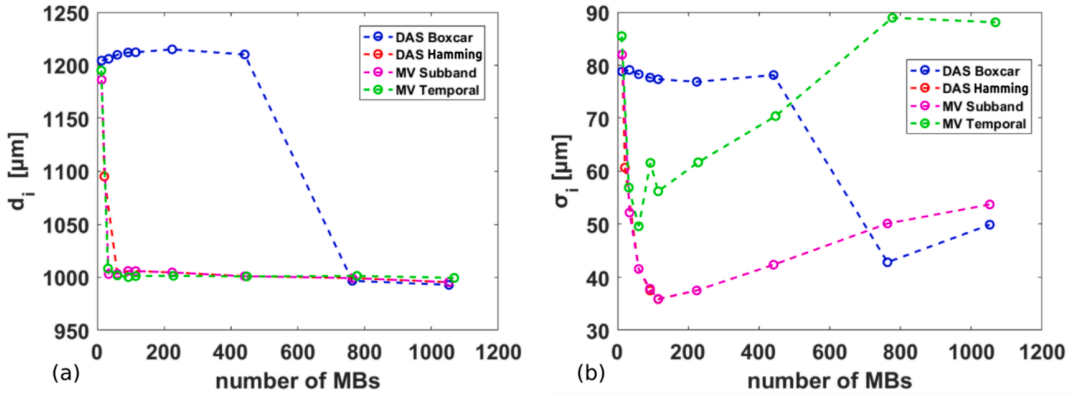

Fig. 9. Effect of data amount (number of MBs) on vessel profiles for a nominal vessel separation of 1000 μm for noiseless data. (a) Estimated vessel distance, (b) standard error of estimated distance.

adjacent microbubble interaction, with consequent deterioration of image quality. Closely spaced MBs are not possible to resolve beyond the diffraction limit, and have main lobe and side lope interactions that may distort PSF morphological characteristics [34]. The large error in detection localisation in these detections generate vessel distortion (Fig. 3) or even artefact vessel structures in between the two vessels (Fig. 7) for both the long duration pulses and DAS beamformers. This explains the observation where the adaptive BF provides reduced false detections in parallel or in crossing vessels for adaptive BFs and as compared to the DAS [25,27]. Therefore, the improved performance of the MV over the DAS is particular to the high number of adjacent MBs, as it was shown that all BFs have very similar localisation performance (Table 2) for well distanced vessels (at 1000 μm) that are well resolved, defined and recognised for all BFs even at high concentrations (Fig. 6). Note, that this analysis is difficult to perform in experimental work due to the absence of particle ground truth location.

Further, the advantage using the MV over the DAS cannot be clearly described as a resolution advantage. As mentioned above, while two microbubbles cannot be resolved beyond the diffraction limit, two vessels can and this is optimal using the MV which performs consistently well for all vessel separation distances, while the DAS deteriorates for separations below 4λ. Vessels beyond a certain distance (here 1000 μm = 5.2λ) provide similar resolution in the ULM maps across all BFs (Fig. 6) as the localisation is similarly accurate and converging to that of a single vessel (Table 2). As the distances between vessels decrease below 4λ there is a superiority for MV BFs (Fig. 6) in localisation uncertainty and sidelobe interaction, as well as in the number of spurious detections, which converts to improvements in vessel definition and separation (Table 3, Fig. 7), as well as avoidance of artefacts. Equally importantly fewer microbubbles are needed for the MV to accurately define vessel separation. The small PSF size and low sidelobes ensure significantly reduced likelihood of interaction and optimal performace similar to that of a single vessel with sparsely located MBs. The large DAS boxcar vessel location error shown in Fig. 9b owes to MB interactions, also explicitly displayed in the example frame of Fig. 3, and thus a statistically larger MB number is required to reduce this error to insignificance. This strongly suggests that *in vivo* networks, containing a mixture of vessel distances, will provide a small improvement in overall resolution for adaptive BFs compared to the DAS ones. This result is confirmed *in vivo* as the MV adaptive BF provided a resolution improvement of 11 % compared to the worse DAS, despite the 4.8-fold narrower lateral FWHM for isolated scatterers, a significantly different resolution performance [27]. As mentioned above, vessels that are several wavelenths apart from the nearest vessel, are likely to be similar in resolution, while others that their neighbouring vessels are below 4λ will have similar resolution by an adaptive beamformer and worse when using the DAS. Note, that the comparative value of the results is of most value here as the absolute values of the measurements are dependent on the specific BF implementations.

The study has a number of limitations. The work here focussed on ULM investigations that deploy the detection and localisation of single MBs. First, the use of detection and localisation methodology introduces systematic uncertainties. It was found that global settings that apply to the data from all BFs do not help assess their performance. The difference in appearance of the image data provided by the different BFs required an ULM algorithm optimised to each specific dataset, which provided the optimal detection/localisation performance for each dataset and the fairest comparison between BFs. Investigations with real data will no doubt introduce further optimisation considerations, given the complex appearance of human vascular anatomy either normal or diseased. Moreover, while here a single methodology for localisation was used, it becomes apparent that in the future the localisation model should be tailored to the beamforming approach. It is however, recognised that real imaging conditions may introduce systematic uncertainty that may be difficult to model and thus new methods to address this out with *in silico* investigations may need to be developed.

A second, related, issue lies with the validation methodology that may introduce further uncertainty. The choice for the acceptance radius of a TD considered here is 1.3λ. In practice this choice trades missed detections with spurious ones and impacts on the value of LU. As an example, the DAS Boxcar method that has elevated side lobes may provide an increase of spurious events. A larger radius, even though it reduces spurious events, results in LU increase. Nevertheless, a reasonable optimal set of parameters both in detection and GT comparison provided a good performance comparison between BFs that will likely be further elucidated when applied to *in vivo* experiments.

Another limitation is that the nonlinear properties of the MBs have not been taken into consideration. To our knowledge, the simulation of MB scatter in realistic imaging conditions is not available. This is because there is a large number of factors that contribute to the MB image, such as the polydispersity of the size and shell property distribution, the wide range of vessel diameters and elastic properties that are hosting the MBs through their journey, the highly variable ultrasound field, and the signal and image processing that generate the ultrasound contrast images. Given that MB physical properties are not well quantified and the MB response to ultrasound not fully understood, the use of a non-linear model to simulate MB response is likely to provide an unknown bias to the signal and image processing result, thus defeating its purpose. For these reasons the factor of non-linearity was not included. We expect that this will not have a significant effect in the comparison between the BFs studied here, and the quantitative nature of the results is a good guide for future development.

A fourth limitation lies in the simplicity of the setup and the fact that this deals with only two parallel straight vessels. The introduction of curvature, bifurcations or crossing vessels of variable widths and arrangements would offer a more realistic setting. However, the aim of the current paper is to simplify the axial and lateral problems, i.e. pulse duration and BF respectively, and the simulation works well by keeping these separate, while a curved vessel scenario would be mixing the two dimensions. Further, the contribution of different BFs to vessel mapping is a problem of the lateral direction only, and the results here link the accuracy in vessel definition and localization to BF performance.

On the other hand a large number of experiments were done in a noiseless environment. Indeed, realistic noise may impact on the performance of the beamformers, while the noise simulation is a complex problem in itself, as a realistic noise is not established in the literature and the topic may well be addressed in a real experiment. The contribution here should therefore be seen as an initial attempt to explain the contribution of a number of factors associated with different PSF appearances to the depiction of vessels. As such a simplified system is deployed with a well recognised simulator (Field II).

As a final comment, and in relation to the above it is important to appreciate that a fundamental limitation of ULM development is the availability of the ground truth itself. This is because the technology has provided a leap in resolution that no other technology is able to match. Both *in vitro* and *in vivo* work cannot easily compare with theoretical studies as the LU validation is not available, and it is currently challenging to build *in vitro* phantoms with vessel distance below a few hundred micrometers, with soft – ultrasound compatible materials, as this is at the resolution limit of 3D printing. As a result, most of the ULM work in the literature focusses on validating vascular topography. *In vivo* work presents additional challenges as there is currently no other technology that can provide validation of live vessel architecture and dimensions for entire organs, and it is known that the fixation process distorts these and thus the validation is qualitative at best.

5. Conclusion

An *in silico* study combined the adaptive MV and the DAS BFs with standard ULM processing in order to investigate and explain the potential gains in deploying adaptive beamformers in super-resolution ultrasound imaging for a high concentration of isolated microbubbles.

It was found that microbubble interaction and spurious detections are the main cause of the deterioration in defining vessels that are separated at distances up to 4λ for the DAS beamformers. Finally, the MV provided robustness of vessel location for small amounts of MB data, which may prove a significant advantage in clinical application. These results confirm and explain previous experimental work.

CRediT authorship contribution statement

Vasiliki Voulgaridou: Investigation. **Barbara Nicolas:** Supervision. **Steven McDougall:** Methodology. **Lachlan Arthur:** Investigation. **Georgios Papageorgiou:** Software. **Mairead Butler:** Methodology. **Evangelos Kanoulas:** Investigation. **Konstantinos Diamantis:** Methodology. **Weiping Lu:** Supervision. **Vassilis Sboros:** Validation, Supervision, Project administration, Conceptualization.

Declaration of competing interest

The authors declare that they have no known competing financial interests or personal relationships that could have appeared to influence the work reported in this paper.

Data availability

The data that has been used is confidential.

Acknowledgement

The authors gratefully acknowledge funding from EPSRC Project grant (EP/N015320/1) titled: “Super-resolution ultrasound” and STFC Project grant (ST/M007804/1) titled: “Imaging the stars from within: Super-resolution contrast ultrasound imaging feasibility”

References

[1] J. Folkman, Angiogenesis in cancer, vascular, rheumatoid and other disease, Nat. Med. 1 (1) (1995) 27–31.
[2] B.V. Zlokovic, Neurovascular pathways to neurodegeneration in Alzheimer’s disease and other disorders, Nat. Rev. Neurosci 12 (12) (2011) 723–738.
[3] D.B. Stanimirovic, A. Friedman, Pathophysiology of the neurovascular unit: disease cause or consequence? J. Cerebral Blood Flow Metabol.: Off. J. Int. Soc. Cerebral Blood Flow Metabol. 32 (7) (2012) 1207–1221.
[4] Capon, J., *High-resolution frequency-wavenumber spectrum analysis.* Proceedings of the IEEE, 1969. **57**(8): p. 1408-1418.
[5] P.M.R.L. Stoica, Spectral analysis of signals. Upper Saddle River, N.J.: Pearson/Prentice Hall, 2005.
[6] J.A. Mann, W.F. Walker, A constrained adaptive beamformer for medical ultrasound: initial results, in: 2002 IEEE Ultrasonics Symposium, 2002. Proceedings. 2002.
[7] J.F. Synnevag, A. Austeng, S. Holm, Adaptive beamforming applied to medical ultrasound imaging, IEEE Trans. Ultrason. Ferroelectrics Frequency Control 54 (8) (2007) 1606–1613.
[8] F. Viola, W.F. Walker, Adaptive signal processing in medical ultrasound beamforming, in: IEEE Ultrasonics Symposium, 2005. 2005.
[9] M. Sasso, C. Cohen-Bacrie. Medical ultrasound imaging using the fully adaptive beamformer, in: Proceedings. (ICASSP ’05). IEEE International Conference on Acoustics, Speech, and Signal Processing, 2005. 2005.
[10] I.K. Holfort, F. Gran, J.A. Jensen, P2B-12 minimum variance beamforming for high frame-rate ultrasound imaging, in: 2007 IEEE Ultrasonics Symposium Proceedings. 2007.
[11] Z. Wang, J. Li, R. Wu, Time-delay- and time-reversal-based robust Capon beamformers for ultrasound imaging, IEEE Trans. Med. Imaging 24 (10) (2005) 1308–1322.
[12] J. Synnevåg, A. Austeng, S. Holm, A low-complexity data-dependent beamformer, IEEE Trans. Ultrason Ferroelectrics Frequency Control 58 (2) (2011) 281–289.
[13] L. Qiu, Y. Cai, M. Zhao, Low-complexity variable forgetting factor mechanisms for adaptive linearly constrained minimum variance beamforming algorithms, IET Signal Proc. 9 (2) (2015) 154–165.
[14] J. Chen, et al., Multi-operator minimum variance adaptive beamforming algorithms accelerated with GPU, IEEE Trans. Med. Imaging 39 (9) (2020) 2941–2953.
[15] S.E. Nai, et al., Iterative robust minimum variance beamforming, IEEE Trans. Signal Process. 59 (4) (2011) 1601–1611.
[16] B.M. Asl, A. Mahloojifar, Contrast enhancement and robustness improvement of adaptive ultrasound imaging using forward-backward minimum variance beamforming, IEEE Trans. Ultrasonics, Ferroelectrics Freq. Control 58 (4) (2011) 858–867.
[17] W. Wang, et al., Adaptive beamforming based on minimum variance (ABF-MV) using deep neural network for ultrafast ultrasound imaging, Ultrasonics 126 (2022) 106823.
[18] Y. Wang, et al., Minimum variance beamforming combined with covariance matrix-based adaptive weighting for medical ultrasound imaging, BioMedical Eng. OnLine 21 (1) (2022) 40.
[19] P. Wang, et al., A high-resolution minimum variance algorithm based on optimal frequency-domain segmentation, Biomed. Signal Process. Control 67 (2021) 102540.
[20] B.W. Ossenkoppele, et al., Improving lateral resolution in 3-D imaging with micro-beamforming through adaptive beamforming by deep learning, Ultrasound Med. Biol. 49 (1) (2023) 237–255.
[21] X. Guo, D. Ta, K. Xu, Frame rate effects and their compensation on super-resolution microvessel imaging using ultrasound localization microscopy, Ultrasonics 132 (2023) 107009.
[22] A. Stanziola, et al., Benefits of Adaptive Beamforming Methods for Contrast Enhanced High Frame-Rate Ultrasound, in: 2018 IEEE International Ultrasonics Symposium (IUS), 2018.
[23] Y. Huang, et al., Improvement of ultrasound contrast imaging with adaptive beamformer based on pulse inversion plane wave transmission, in: 2016 URSI Asia-Pacific Radio Science Conference (URSI AP-RASC), 2016.
[24] H. Zhang, et al., Multibeam minimum variance beamforming for ring array ultrasound imaging, Phys. Med. Biol. 68 (13) (2023) 135005.
[25] R. Tasbaz, B.M. Asl, Improvement of microbubbles localization using adaptive beamforming in super-resolution ultrasound imaging, in: 2021 IEEE International Ultrasonics Symposium (IUS). 2021.
[26] R. Tasbaz, B.M. Asl, Super-resolution ultrasound imaging with low number of frames enhanced by adaptive beamforming, in: 2021 IEEE International Ultrasonics Symposium (IUS). 2021.
[27] J. Yan, et al., Fast 3D super-resolution ultrasound with adaptive weight-based beamforming, IEEE Trans Biomed Eng 70 (9) (2023) 2752–2761.
[28] M.J. Dill-Macky, et al., Focal hepatic masses: enhancement patterns with SH U 508A and pulse-inversion US, Radiology 222 (1) (2002) 95–102.
[29] L. Prantl, et al., Value of high resolution ultrasound and contrast enhanced US pulse inversion imaging for the evaluation of the vascular integrity of free-flap grafts, Clin Hemorheol Microcirc 36 (3) (2007) 203–216.
[30] G.A.A. Brock-fisher, Mckee D. Poland, Patrick G. Rafter, Means for increasing sensitivity in non-linear ultrasound imaging systems, in Hewlett-Packard Company (Palo Alto, CA), United States, 1996.
[31] K. Thomenius, Evolution of ultrasound beamformers 2 (1996) 1615–1622.
[32] V. Perrot, et al., So you think you can DAS? A viewpoint on delay-and-sum beamforming, Ultrasonics 111 (2021) 106309.
[33] V. Sboros, et al., The behaviour of individual contrast agent microbubbles, Ultrasound. Med. Biol. 29 (5) (2003) 687–694.
[34] K. Diamantis, et al., Resolving ultrasound contrast microbubbles using minimum variance beamforming, IEEE Trans. Med. Imaging 38 (1) (2019) 194–204.
[35] K. Diamantis, et al., Experimental performance assessment of the sub-band minimum variance beamformer for ultrasound imaging, Ultrasonics 79 (2017) 87–95.
[36] K. Christensen-Jeffries, et al., Super-resolution ultrasound imaging, Ultrasound Med. Biol. 46 (4) (2020) 865–891.
[37] Y. Desailly, et al., Resolution limits of ultrafast ultrasound localization microscopy, Phys. Med. Biol. 60 (22) (2015) 8723–8740.
[38] I.K. Holfort, F. Gran, J.A. Jensen, Broadband minimum variance beamforming for ultrasound imaging, IEEE Trans Ultrason Ferroelectr Freq Control 56 (2) (2009) 314–325.
[39] J. Zhao, et al., Subarray coherence based postfilter for eigenspace based minimum variance beamformer in ultrasound plane-wave imaging, Ultrasonics 65 (2015).
[40] N.Q. Nguyen, R.W. Prager, Minimum variance approaches to ultrasound pixel-based beamforming, IEEE Trans. Med. Imaging 36 (2) (2017) 374–384.
[41] O.M.H. Rindal, et al., Understanding contrast improvements from capon beamforming. In 2014 IEEE International Ultrasonics Symposium, 2014.
[42] K. Christensen-Jeffries, et al., Poisson statistical model of ultrasound super-resolution imaging acquisition time, IEEE Trans. Ultrason. Ferroelectr. Freq. Control 66 (7) (2019) 1246–1254.
[43] V. Hingot, et al., Microvascular flow dictates the compromise between spatial resolution and acquisition time in Ultrasound Localization Microscopy, Sci. Rep. 9 (1) (2019) 2456.
[44] S. Dencks, M. Piepenbrock, G. Schmitz, Assessing vessel reconstruction in ultrasound localization microscopy by maximum likelihood estimation of a zero-inflated poisson model, IEEE Trans. Ultrason. Ferroelectrics Freq. Control 67 (8) (2020) 1603–1612.
[45] S. Mehdizadeh, et al., Eigenspace based minimum variance beamforming applied to ultrasound imaging of acoustically hard tissues, IEEE Trans. Med. Imaging 31 (10) (2012) 1912–1921.
[46] A. Boujelben, et al., Multimodality imaging and mathematical modelling of drug delivery to glioblastomas, Interface Focus 6 (5) (2016).
[47] J.A. Jensen, Field: a program for simulating ultrasound systems, Med. Biol. Eng. Compu. 34 (sup. 1) (1997) 351–353.
[48] J.A. Jensen, N.B. Svendsen, Calculation of pressure fields from arbitrarily shaped, apodized, and excited ultrasound transducers, IEEE Trans. Ultrason. Ferroelectr. Freq. Control 39 (2) (1992) 262–267.
[49] J.A. Jensen, et al., SARUS: A synthetic aperture real-time ultrasound system, IEEE Trans. Ultrasonics Ferroelectrics Frequency Control 60 (9) (2013) 1838–1852.

[50] E. Kanoulas, et al., Super-resolution contrast-enhanced ultrasound methodology for the identification of in vivo vascular dynamics in 2D, Invest. Radiol. 54 (8) (2019) 500–516.
[51] X. Yang, H. Li, X. Zhou, Nuclei segmentation using marker-controlled watershed, tracking using mean-shift, and kalman filter in time-lapse microscopy, IEEE Trans. Circuits Syst. I Regul. Pap. 53 (11) (2006) 2405–2414.
[52] K. Christensen-Jeffries, et al., Microbubble Axial localization errors in ultrasound super-resolution imaging, IEEE Trans. Ultrason. Ferroelectr. Freq. Control 64 (11) (2017) 1644–1654.
[53] D.H. Thomas, et al., Single microbubble response using pulse sequences: initial results, Ultrasound Med. Biol. 35 (1) (2009) 112–119.
[54] K. Diamantis, et al., Super-resolution axial localization of ultrasound scatter using multi-focal imaging, IEEE Trans. Biomed. Eng. 65 (2018) 1840–1851.
[55] G. Russo, et al., Angiogenesis in prostate cancer: onset, progression and imaging. BJU Int **110**(11 Pt C) (2012) E794-808.